Top of the Atmosphere Reflected Shortwave Radiative Fluxes from GOES-R

Rachel T. Pinker[1], Yingtao Ma[1], Wen. Chen[1], Istvan Laszlo[2], Hongqing Liu[3],
Hye-Yun Kim[3] and Jamie Daniels[2]

[1] Department of Atmospheric and Oceanic Science, University of Maryland, College Park, MD

[2] NOAA NESDIS Center for Satellite Applications and Research, College Park, MD

[3] I.M. Systems Group, Inc., Rockville, MD

Correspondence to: Rachel T. Pinker (pinker@atmos.umd.edu)

Abstract. Under the GOES-R activity, new algorithms are being developed at the National Oceanic and Atmospheric Administration (NOAA)/Center for Satellite Applications and Research (STAR) to derive surface and Top of the Atmosphere (TOA) shortwave (SW) radiative fluxes from the Advanced Baseline Imager (ABI), the primary instrument on GOES-R. This paper describes a support effort in the development and evaluation of the ABI instrument capabilities to derive such fluxes. Specifically, scene dependent narrow-to-broadband (NTB) transformations are developed to facilitate the use of observations from ABI at the TOA. Simulations of NTB transformations have been performed with MODTRAN4.3 using an updated selection of atmospheric profiles and implemented with the final ABI specifications. These are combined with Angular Distribution Models (ADMs), which are a synergy of ADMs from the Clouds and the Earth's Radiant Energy System (CERES) and from simulations. Surface condition at the scale of the ABI products as needed to compute the TOA radiative fluxes come from the International Geosphere-Biosphere Programme (IGBP). Land classification at 1/6 $^{\circ}$ resolution for 18 surface types are converted to the ABI 2-km grid over the (CONtiguous States of the United States) (CONUS) and subsequently re-grouped to 12 IGBP types to match the classification of the CERES ADMs. In the simulations, default information on aerosols and clouds is based on the ones used in MODTRAN.

27 Comparison of derived fluxes at the TOA is made with those from CERES. A satisfactory agreement

28 between the fluxes was observed for both clear and cloudy conditions and possible reasons for differences

29 have been identified**.**

31 **1. Introduction**

33 One of the objectives at NOAA/STAR in respect to the utilization of observations from the Advanced

34 Baseline Imager (ABI) is to be able to derive shortwave (SW↓) radiative fluxes at the surface. To get to

35 the surface SW↓ from TOA satellite observations, there are two generic approaches: 1) the direct approach

36 and 2) the indirect approach. In the direct approach one uses all the necessary information needed for

37 deriving the surface fluxes (some of which can be derived from satellites). Implementation of such an

38 approach is feasible, for instance, with observations from MODIS which has a long history of product

39 availability and evaluation. Examples are illustrated in Wang and Pinker (2009), Niu and Pinker, (2015),

40 Ma et al. (2016), Pinker et al. (2018), Pinker et al., (2017a), Pinker et al. (2017b). GOES-R is a new

41 instrument and as yet, similar information to the one from MODIS is not yet available. Therefore, the

42 indirect approach is used where one starts from satellite observations at the TOA and models the

43 atmosphere and surface with best available information (which does not have to be based on ABI).

44 Examples of such an approach are discussed in Pinker, Zhang and Dutton (2005), Ma and Pinker (2012)

45 and Zhang et al. (2019). The "indirect path method" is used at the Center for Satellite Applications and

46 Research (STAR) (Laszlo et al., 2020) for deriving SW↓ radiative fluxes from satellite observations; it

47 requires knowledge of the SW broadband (0.2 – 4.0 µm) top of the atmosphere (TOA) albedo. The

48 Advanced Baseline Imager (ABI) observations onboard of the NOAA GOES-R series of satellites provide

49 reflectance in six narrow bands in the shortwave spectrum (**Table 1**); these must be first transformed into

50 broadband reflectance (the NTB conversion), and the broadband reflectance must be transformed into a

51 broadband albedo (the ADM conversion). During the pre-launch activity NTB transformations were

52 developed based on theoretical radiative transfer simulations with MODTRAN-3.7 and 14 land use

53 classifications from the International Geosphere-Biosphere Programme (*IGBP*) *(*Hansen et al., 2010*)*.

54 They were augmented with ADMs from (CERES) observed ADMs (Loeb et al., 2003) and theoretical

55 simulations (Niu and Pinker, 2011) to compute TOA fluxes. The resulting NTB transformations and

56 ADMs have been tested using proxy data and simulated ABI data. The proxy instruments used in these

57 early simulations include the GOES-8 satellite, the Advanced Very-High Resolution Radiometer

58 (AVHRR) sensor on the Polar Orbiting satellites, the Spinning Enhanced Visible Infra-Red Imager

59 (SEVIRI) sensor on the European METEOSAT Second Generation (MSG) satellites, and the Moderate

60 Resolution Imaging Spectroradiometer (MODIS) instrument on the NASA Terra and Aqua Polar Orbiting

61 satellites (Pinker et al*.,* 2021, unpublished). For each of these satellites, the evaluation of the

62 methodologies was done differently; some results were evaluated against ground observations while

63 others, against TOA information from CERES as well as from the (ESA) Geostationary Earth Radiation

64 Budget (GERB) satellite (Harries et al., 2005). The results obtained provided an insight on the expected

65 performance of the new ABI sensor. Those procedures have been subsequently updated and applied to

66 the new ABI instrument once it was built and fully characterized.

67 In this paper we describe activity in support of the effort to derive surface shortwave (SW↓) radiative

68 fluxes from the operational Advanced Baseline Imager (ABI) instrument on the GOES-R series of the

69 NOAA geostationary meteorological satellites using the latest version of the ABI data. We describe the

70 physical basis and the development of the (NTB) transformations of satellite observed radiances and the

71 bi-directional corrections to be applied to the broadband reflectance to obtain broadband TOA albedo.

72 The methodology will be presented in section 2, data used are described in section 3, results in section 4

73 and a summary and discussion in section 5.

74

75 **2. Methodology**

76

77 The following two flowcharts (**Figs. 1 and 2**) describe the necessary steps to derive the NTB

78 transformations and the ADMs. Details on these two steps will follow.

79 The TOA narrowband and broadband reflectance can be calculated from the spectral radiances

80 simulated from MODTRAN 4.3 and the response functions of the satellite sensor as shown in equations

81 (1) and (2):

82
$$\rho_{nb}(\theta_0,\theta,\phi) = \frac{\pi \int_{\lambda1}^{\lambda2} I(\lambda,\theta_0,\theta,\phi)G(\lambda)d\lambda}{\int_{\lambda1}^{\lambda2} \cos(\theta_0)S_0(\lambda)G(\lambda)d\lambda} \qquad (1)$$

83
$$\rho_{bb}(\theta_0,\theta,\phi) = \frac{\pi \int_{0.2\,\mu m}^{4\,\mu m} I(\lambda,\theta_0,\theta,\phi)d\lambda}{\int_{0.2\,\mu m}^{4\,\mu m} \cos(\theta_0)S_0(\lambda)d\lambda} \qquad (2)$$

84

85 where ρ_{nb} is narrowband reflectance; ρ_{bb} is broadband reflectance; θ_0: solar zenith angle; θ: view

86 (satellite) zenith angle; ϕ: relative azimuth angle;

87 I_λ: reflected spectral radiance; $S_0(\lambda)$: solar spectral irradiance;

88 G_λ: spectral response functions of satellite sensors; λ_1 and λ_2 are the spectral limits of the sensor spectral

89 band. This approach is widely used in the scientific community as also implemented in the work of Loeb

90 et al (2005), Wielicki et al. (2008), Su et al. (2015) and Akkermans et al. (2020).

91 As stated previously, the ADMs from CERES-based observations (Loeb et al., 2005; Kato et al. 2015)

92 were augmented with theoretical simulations (Niu and Pinker, 2011) to compute TOA fluxes. This was

93 done since CERES observations at that time were under-sampled. at higher latitudes.

94 The combined ADMs are developed for each angular bin by weighting the modeled and CERES ADMs

95 based on the number of samples used to derive the ADMs of each type (Niu et al., 2011). Specifically:

96
$$\bar{R}(\theta_0,\theta,\phi) = \frac{1}{m+n}\left(m \times R_{CERES}(\theta_0,\theta,\phi) + n \times R_S(\theta_0,\theta,\phi)\right) \tag{3}$$

97   $\bar{R}(\theta_0,\theta,\phi)$:   averaged ADMs at each angular bin;

98   R_{CERES}:   anisotropic factor from CERES ADMs;

99   R_S: anisotropic factor from simulated ADMs;

100   m and n: observation numbers at angular bins for CERES and simulated ADMs.

101

2.1 Selection of Atmospheric profiles for simulations

103

104   We have selected 100 atmospheric profiles covering the globe and the seasons as input for simulations
105   with MODTRAN4.3. The atmospheric profiles at each pressure level include temperature, water vapor
106   and ozone. Each season includes 25 profiles. A tool was developed to select profiles from a Training Data
107   set known as SeeBor Version 5.0 (https://cimss.ssec.wisc.edu/training_data/) (Borbas et.al. 2005).
108   Originally it consisted of 15704 global profiles of temperature, moisture, and ozone at 101 pressure levels
109   for clear sky conditions. The profiles are taken from NOAA-88, and the European Centre for Medium-
110   Range Weather Forecasts (ECMWF) 60L training set, TIGR-3, ozone-sondes from 8 NOAA Climate
111   Monitoring and Diagnostics Laboratory (CMDL) sites, and radiosondes from the Sahara Desert during
112   2004. A technique to extend the temperature, moisture, and ozone profiles above the level of existing data
113   was also implemented by the providers (University of Wisconsin-Madison, Space Science and
114   Engineering Center, Cooperative Institute for Meteorological Satellite Studies (CIMSS). **Fig. 3** shows the
115   location of the selected profiles.
116   The SeeBor profiles are clear sky profiles. The top of the profiles is at 0.005 mb which is about 82.6 km.
117   We did an experiment to check the impact of reducing the number of levels for a profile (initially, we
118   have used only 40 levels). In the experiment computed were radiances from profiles with 50 levels as

119 well as radiances from profiles with 98 Levels. The difference between the two radiances (50 lev-98 lev)

120 were below 5 % reaching 15 % around 2.5 μm. In the experiment we used the odd number levels starting

121 from surface (plus the highest level) to reduce the number of profile levels. Based on these experiments

122 we have opted to keep all 98 profile levels.

123 The surface variables we have used are from MODIS and include surface skin temperature, 2 m

124 temperature, land/sea mask, and albedo. We have conducted a thorough investigation how the selected

125 profiles represent the entire sample of 15704 profiles. An example showing the comparison of

126 temperature, humidity and ozone profiles is shown in **Fig. 4.** As seen, there is a positive bias in the selected

127 profile of temperature due to their higher concentration at the lower latitudes. A positive bias can be found

128 at the lower levels while a negative bias is seen above 1 mb. Since our domain of study is in such latitudes

129 this selection should not have adverse effects on the simulations performed.

130

131 **2.2 Surface conditions**

132

133 Surface condition is one of the primary inputs into the MODTRAN simulations. The International

134 Geosphere-Biosphere Programme (IGBP) land classification is used as a source (Hansen et al., 2010;

135 Loveland et al., 2010). The dataset is at 1/6-degree resolution and includes 18 surface types. We have

136 converted the 1/6º (~18.5 km) resolution to the ABI 2-km grid using the nearest grid method (**Fig. 5**). The

137 surface type is fixed in time. The method for cloudy sky uses 4 surface types; these are also derived from

138 12 IGBP types (**Table 2**).

139

140 **2.3 Clear and cloudy sky simulations**

141

142 Under clear sky, scattering from aerosols is important. We have included 6 aerosol types (**Table 3**) to

143 cover a range of possible conditions under clear sky. Aerosol models are selected based on the type of

144 extinction and a default meteorological range for the boundary-layer aerosol models as listed below:

145 Aerosol Type 1: Rural extinction, visibility = 23 km

146   Aerosol Type 4: Maritime extinction, visibility = 23 km

147   Aerosol Type 5: Urban extinction, visibility = 5 km

148   Aerosol Type 6: Tropospheric extinction, visibility = 50 km

149   Aerosol Type 8: Advective Fog extinction, visibility = 0.2 km

150   Aerosol Type 10: Desert extinction for default wind conditions

151   For the 6 aerosol types, the total number of MODTRAN simulations for each surface type is 462,000. It

152   is obtained as follows: 6 aerosol types x 100 profiles x 770 angles.

153   When performing NTB simulations, we use all 6 types of aerosols. The Rural, Ocean, Urban and Fog

154   aerosols are distributed in the lower 0-2 km region. Tropospheric aerosol is distributed from 0 to 10 km

155   tropopause. The Rural, Ocean, Urban and Tropospheric aerosol optical properties have Relative Humidity

156   (RH) dependency. The Single Scattering Albedo (SSA) is given on 4 RH grids (0, 70, 80, 99) on a spectral

157   grid of 788 points ranging from 0.2 to 300 microns.

158   Simulations were performed for ABI for all the cloud cases described in **Table 3.** To merge cloud layers

159   with atmospheric profiles we have followed the procedure as described in *Berk et al.* (1985, 1998),

160   namely: "Cloud profiles are merged with the other atmospheric profiles (pressure, temperature, molecular

161   constituent, and aerosol) by combining and/or adding new layer boundaries. Any cloud layer boundary

162   within half a meter of an atmospheric boundary layer is translated to make the layer altitudes coincide;

163   new atmospheric layer boundaries are defined to accommodate the additional cloud layer boundaries."

164   100% relative humidity is assumed within the cloud layers (default).

165

166   **2.4 Selection of angles**

167

168   The total number of angles used in the simulations is given in **Table 4**. The selected spectral grids for

169   solar zenith angles, satellite view angles and relative azimuth angles are at Gaussian quadrature points,

170   plus 0° to solar zenith angles (sza) and satellite viewing angles (vza) and 0° and 180° (forward and

171   backward view) to the satellite relative azimuth angles. Solar angle and satellite view angle are referenced

172 to target or surface for satellite simulation with 0° meaning looking up (zenith). Relative azimuth angle is

173 defined as when the relative azimuth angle equals 180°, the sun is in front of observer.

174 The definitions of solar zenith angle and azimuth angle in this table corresponds to the definitions of

175 MODTRAN but that is not the case for the satellite zenith angle. MODTRAN uses nadir angle as 180°-

176 satellite zenith angle, ignoring spherical geometry.

177

178 **2.5 Selection of optimal computational scheme**

179

180 MODTRAN4.3 provides three multiple scattering models (Isaacs, DISORT, and Scaled Isaacs) and three

181 band models at resolutions (1 cm^{-1}, 5 cm^{-1}, and 15 cm^{-1}). The DISORT model (Stamnes et al., 1988)

182 provides the most accurate radiance simulations but the runs are very time consuming. The Isaacs (Isaacs

183 et al. 1987) 2-stream algorithm is fast but oversimplified. The Scaled Isaacs method performs radiance

184 calculations using Isaacs 2-stream model over full spectral range and using DISORT model at a small

185 number of atmospheric window wavelengths. The multiple scattering contributions for each method are

186 identified and ratios of the DISORT and Isaacs methods are computed. This ratio is interpolated over the

187 full wavelength range, and finally, applied as a multiple scattering scale factor in a spectral radiance

188 calculation performed with the Isaacs method.

189 To optimize simulation speed and accuracy, we performed various sensitivity tests, including

190 combinations of multiple scattering models, band resolution, and number of streams. **Table 5** lists

191 simulation options and their corresponding calculation speed.

192 Based on results presented in **Table 5**, the efficient options (< 40 seconds) are Isaacs, DISORT 2-stream

193 with 15 cm^{-1}, DISORT 4-stream 15 cm^{-1}, and Scaled Isaacs all streams at all resolutions. Although the

194 ideal option is DISORT 8-stream with 1 cm^{-1} resolution, there is a trade-off between speed and accuracy.

195 **Fig. 6** compares DISORT simulated radiances at three band resolutions. We use two spectral ranges of

196 0.4 – 0.5 µm and 1.5 – 2.0 µm to illustrate differences. **Fig. 6** shows that the coarser band resolution has

197 smoothed out the radiance variations. The 15 cm^{-1} has the smoothest curve among the three, and 1 cm^{-1}

198 shows more variations than the other two. Another (scientific) criteria for selecting the spectral resolution

199   is the ability to resolve/match the relative spectral response function (SRF) of a sensor. For example, the

200   SRFs of channels 1-6 of ABI are given at every 1 cm^{-1}.

201   Accordingly, we have chosen the 1 cm^{-1} band model for the MODTRAN radiance simulations. Performed

202   were also radiance simulations from different multiple scattering models at 1 cm^{-1} resolution. The whole

203   spectrum of 0.2 – 4 µm was separated to 14 sections so that the differences can be assessed clearly. For

204   wavelength below 0.3 µm and beyond 2.5 no discernible differences were found among Isaacs, DISORT

205   2-, 4-, and 8-strem, and Scaled Isaac. The largest differences occurred in the spectral range of 0.4 – 1.0

206   µm. Scaled Isaac 8-stream follows DISORT 8-stream closely across the whole spectral range; the Scaled

207   Isaac method provided near-DISORT accuracy with the speed of Isaacs. Thus, the MODTRAN4.3

208   simulations for GOES-R ABI were set-up with Scaled Isaac 8-stream with 1 cm^{-1} band resolution.

209   For illustration, in **Fig. 7** compared are radiances simulated by Isaac 2 stream, Scaled Isaac, and DISORT-

210   4 stream for the case of Relative Azimuthal Angle=1.9º, View Angle=76.3º, Solar Zenith Angle=87.2º.

211   The lines are differences between various settings and DISORT-8 stream (e.g. Isaacs minus DISORT-8).

212   Isaac has the least accuracy since it is oversimplified, 4-stream showed some improvements when

213   compared with Isaac while still has large differences for 0.4 µm and is still computationally demanding.

214   Scaled Isaac provides the smallest differences between DISORT-8. **Fig. 7** (lower) zoomed in to the large

215   difference area of 0.3-0.35 µm which indicates that Scaled Isaacs still provides satisfactory results.

216

217   **2.6 Regression methodologies**

218

219   We have derived coefficients of regression using a constrained least-square curve fitting methods of

220   Matlab, "lsqnonneg", which can solve a linear or nonlinear least-squares (data-fitting) problem and

221   produce non-negative coefficients. Non-negative coefficients avoid generating negative TOA flux, which

222   is not a physically valid.

223   To ensure that information from all channels is used and avoid the complex cross-correlation problem, it

224   was opted to generate Narrow to Broad (NTB) coefficients for each ABI channel separately. These

225   channel specific NTB coefficients are applied to each channel to convert ABI narrow-band reflectance to

226 extended band. The final broad-band TOA reflectance is taken as the weighted sum of all 6-channel

227 specific broad-band reflectance. The logic behind this approach is the assumption that the narrow-band

228 reflectance from each channel is a good representative for a limited spectral region centered around the

229 channel and the total spectral reflectance is dominated by the spectral region that contains the most solar

230 energy.

231 To generate "separate-channel" NTB coefficients, each narrow-band ABI channel reflectance is

232 converted to a reflectance $\rho_{bb,i}$ separately,

233 $$\rho_{bb,i}(\theta_0, \theta, \phi) = c_{0,i}(\theta_0, \theta, \phi) + c_{1,i}(\theta_0, \theta, \phi) * \rho_{nb,i}(\theta_0, \theta, \phi) \qquad (4)$$

234 where $\rho_{bb,i}$ is the band reflectance for an interval around each channel i; $c_{0,i}$ and $c_{1,i}$ are regression

235 coefficients for channel i. These regression coefficients are derived separately for various combination of

236 surface, cloud and aerosol types. The total shortwave broad band ($0.25 - 4.0\mu$m) reflectance ρ_{bb}^{est} is

237 obtained by taking the weighted sum of all 6 $\rho_{bb,i}$ reflectance

238 $$\rho_{bb}^{est}(\theta_0, \theta, \phi) = \sum_i \rho_{bb,i}(\theta_0, \theta, \phi) \frac{S_{0,i}}{S_0} \qquad (5)$$

239 Here, S_0 and $S_{0,i}$ are total solar irradiance and band solar irradiance for each channel, respectively. Band

240 edges around the six ABI channels are: 49980-18723, 18723-13185, 13185-9221, 9221-6812, 6812-5292,

241 2500 cm^{-1} 0.2001-0.5341, 0.5341-0.7584, 0.7584-1.0845, 1.0845-1.4680, 1.4680-1.8896, 1.8896-4.0000

242 μm). The corresponding solar irradiance band values are 364, 360, 287, 168, 91, 87

243 W m^{-2}. **Fig. 8** shows the sensor response function (SRF) and locations of the six ABI channels.

244 Coefficients are generated for clear condition and 3 types of cloudy conditions. Comparison between ABI

245 TOA flux and CERES products are shown in **Fig. 9**. The "separate-channel" coefficients work well for

246 predominantly clear sky (**Fig.10**). Differences are somewhat more scattered for cloudy cases. The reason

247 may be due to the fact that the ABI observation time and CERES product time do not match perfectly

248 since cloud condition change quickly. As discussed in Gristey et al. (2019) there are SW spectral

249 reflectance variations for different cloud types. Possibly, for ABI bands some spectral variations

250 associated with cloud variability are missed. It is important to have the correct cloud properties to be able

251 to select correct ADM. Misclassification of cloud properties will therefore result in flux differences. They

252 also argue that ADMs have an uncertainty due to within-scene variability and within-angular bin
253 variability leading to additional flux differences.
254
255 **3. Data used**
256
257 **3.1 Satellite data for GOES-16 and GOES17**
258
259 The GOES Imager data used **(Table 6)** were downloaded from https://www.bou.class.noaa.gov/ and the
260 SRF from https://ncc.nesdis.noaa.gov/GOESR/ABI.php
261 The CODC data were not always available from CLASS and had to be obtained from NOAA/STAR
262 temporary archives. Also, not all the required angular information needed for implementation of
263 regressions was available online and had to be recomputed.
264
265 **3.2 Reference data from CERES**
266
267 The CERES Single Scanner Footprint (SSF) is a unique product for studying the role of clouds, aerosols,
268 and radiation in climate. Each CERES footprint (nadir resolution 20-km equivalent diameter) on the SSF
269 includes reflected shortwave (SW), emitted longwave (LW) and window (WN) radiances and top-of-
270 atmosphere (TOA) fluxes from CERES with temporally and spatially coincident imager-based radiances,
271 cloud properties, and aerosols, and meteorological information from a fixed 4-dimensional analysis
272 provided by the Global Modeling and Assimilation Office (GMAO). Each file in this data product
273 contains one hour of full and partial-Earth view measurements or footprints at a surface reference level.
274 Detailed information can be found via https://ceres.larc.nasa.gov/data/#ssf-level-2.
275 Near real-time CERES fluxes and clouds in the SSF format are available within about a week of
276 observation (Kratz et al., 2014). They do not use the most recent CERES instrument calibration and thus

contains some uncertainty. Before GOES data were transferred to the Comprehensive Large Array-data

Stewardship System (CLASS) system, the NOAA/STAR archive was holding new data for about a week.

Therefore, the initial evaluations had to be done only with data that overlapped in time. The CERES data

known as the FLASHFlux Level2 (FLASH_SSF) are available almost in real time from:

https://ceres.larc.nasa.gov/products.php?product=FLASHFlux-Level2

Due to such constraints the early comparison was done between ABI data as archived at NOAA/STAR

and the FLASHFlux products (in this paper, the FLASHFlux data were used only in Fig. 9). The archiving

of GOES-R at the NOAA Comprehensive Large Array-data Stewardship System (CLASS) started only

in 2019, however, it contains data starting from 2017. Once the CLASS archive became available, we

have augmented GOES-16 cases with observations from GOES-17; only those cases will be shown in this

paper.

3.3 Data preparation

For the re-mapping, we adopted the ESMF re-gridding package. The detailed information can be found

at: http://earthsystemmodeling.org/regrid/

For an ideal situation, the ABI high-resolution TOA SW fluxes should be mapped into the CERES

footprint for validation. However, there are reasons that make it difficult to do so. There can be more than

18000 pixels in a single swath of the SSF, when constrained to U.S. Different pixels have different times.

Neglecting the seconds, there are still more than 30 mins differences (this changes case by case) between

297   the first pixel and the one at the end and this brings up a time matching issue. By remapping the SSF to

298   ABI, we can set up a unique time for ABI (ABI is at 5 min intervals) and then constrain the region and

299   the time range of SSF.

300   Both re-mapping the ABI to SSF and remapping SSF to the ABI bring up spatial matching errors as

301   recognized by the scientific community (Rilee and Kuo, 2018; Ragulapati et al., 2021). In **Fig. 11**, we

302   show the SSF before re-gridding (**Figs 11 (a) & (b)**) and after re-gridding (**Figs. 11 (c) and (d)).** The

303   fluxes after re-mapping CERES SSF to the ABI resolution resemble well the original structure. Another

304   consideration is the computational efficiency of re-mapping the curvilinear tripolar grid to unconstructed

305   grid. For large arrays, it is more efficient to remap the unconstructed grid to the curvilinear tripolar grid.

306

307   **4. Results**

308

309   **4.1 Comparison between ABI TOA fluxes to those from CERES SSF**

310   A case for 2019/12/26 (doy 360) UTC 19:36 is illustrated in **Figs. 11-14.** Statistical summaries from an
311   extended number of cases that cover all four seasons are presented in **Table 7**.
312   We have conducted several experiments to select an appropriate regression approach to the NTB
313   transformation ensuring that non-physical results are not encountered. Based on the samples used in this
314   study **(Table 7)** the differences found for Terra and GOES-16 were in the range of -0.5-(-17.37) for bias
315   and 43.28-81.72 for standard deviation; for Terra and GOES-17 they were 11.26-47.09 and 70.25-108.73,
316   respectively. For Aqua and GOES-16 they were 7.63-33.87and 58.68-117.43 respectively while for Aqua
317   and GOES-17 they were 0.19-31.53 and 47.55-129.42, respectively (all units are W m^{-2}). The evaluation
318   process revealed the challenges in undertaking such comparisons. Both estimates of TOA fluxes (CERES
319   and GOES) do no account for seasonality in the land use classification; the time matching for the different

satellites is important and limits the number of samples that can be used in the comparison. Based on the results of this study recommendation for future work include the need to incorporate seasonality in land use and spectral characteristic of the various surface types. Possible stratification by season in the regressions could also be explored.

4.2 Causes for differences between ABI and CERES TOA fluxes

4.2.1 Differences in surface spectral reflectance

In the MODTRAN simulations we use the spectral reflectance information on various surface types as provided by MODTRAN. MODTRAN version 4.3.1 contains a collection of spectral surface reflectance dataset from the Moderate Spectral Atmospheric Radiance and Transmittance (MOSART) model (Cornette et al., 1994) and others from Johns Hopkins University Spectral Library (Baldridge et al., 2009). When doing simulation, we call the built-in surface types and use the provided surface reflectance. As such, the spectral dependence of the surface reflectance used in the simulations and matched to the CERES surface types may not be compatible with the classification of CERES. Also, seasonal changes in surface type classification can introduce errors due to changes in the spectral surface reflectance for different surface types (**Fig. 15).**

4.2.2 Issues related to surface classification

Another possible cause for differences between the TOA fluxes is the classification of surface types as originally identified by the IGBP and used in the simulations. No seasonality is incorporated in the surface type classification while such variability is part of the CERES observations.

4.2.3 Issues related to match-up between GOES-R and CERES

Both Terra and Aqua have sun-synchronous, near-polar circular orbits. Terra is timed to cross the equator from north to south (descending node) at approximately 10:30 am local time. Aqua is timed to cross the equator from south to north (ascending node) at approximately 1:30 pm local time. The periods for Terra and Aqua are 99 and 98 minutes, respectively. Both have 16 orbits per day. CERES on Terra and Aqua optical FOV at nadir is 16 x 32 or 20 km resolution. Terra passes CONUS during 03-06 UTC (US night time), 16-20 UTC (US day time), and Aqua passes CONUS during 07-11 UTC (US night time), 18-22 UTC (US day time).

Both Terra and Aqua have an instantaneous FOV values at SWATH level. There is no perfect overlap, temporally or spatially with ABI data. The ABI radiance and cloud data are on a regular grid of 2*2 km over CONUS at each hour. To use CERES data for evaluation of ABI, there is a need to perform collocation in both time and space.

5. Summary

The derivation and evaluation of TOA radiative fluxes as simulated for any given instrument are quite challenging. In principle, there is a need to account for all possible changes in the atmospheric and surface conditions one may encounter in the future. Yet, to know what these conditions are at the time of actual observation when there is a need to select the appropriate combination of variables from the simulations, is a formidable task. Differences in assumed cloud properties can also lead to differences in the fluxes derived from the two instruments. Therefore, error can be expected due to discrepancies between the actual conditions and the selected simulations and these are difficult to estimate. The approach we have selected is based on high-quality simulations using a proven and accepted radiative transfer code (MODTRAN) of known configurations and a wide range of atmospheric conditions. We have also selected the best available estimates of TOA radiative fluxes from independent sources for evaluation. However, the matching between different satellites in space and time is challenging. In selecting the cases

374 for evaluation, we have adhered to strict criteria of time and space coincidence as described in section

375 3.3.

376 Critical elements of an inference scheme for TOA radiative flux estimates from satellite observations are:

377 1) transformation of narrowband quantities into broadband ones;

378 2) transformation of bi-directional reflectance into albedo by applying Angular Distribution Models

379 (ADMs). In principle, the order in which these transformations are executed is arbitrary. However, since

380 well established, observation-based broadband ADMs derived from the Clouds and the Earth's Radiant

381 Energy System (CERES) project already exist, the logical procedure is to do the NTB transformation on

382 the radiances first, and then apply the ADM. This is the sequence that has been followed here. While the

383 road map to accomplish above objectives seems well defined, reaching the final goal of having a stable

384 up-to-date procedure for deriving TOA radiative fluxes from a new instrument like the ABI on the new

385 generation of GOES satellites is quite complicated. Since the final configuration of the instrument

386 becomes known at a much later stages the evaluation of new algorithms is in a fluid stage for a long time

387 so early evaluation against "ground truth" needs to be repeated frequently. Additional complication is

388 related to the lack of maturity of basic information needed in the implementation process, such as a

389 reliable cloud screened product which in itself is in a process of development and modifications. The

390 "ground truth", namely, the CERES observations are also undergoing adjustments and recalibration. As

391 such, the process of deriving best possible estimates of TOA radiative fluxes from ABI underwent

392 numerous iterations to reach its current status. An effort was made to deal the best way possible with the

393 fluid situation. All the evaluations against CERES were repeated once the ABI data reached stability and

394 were archived in CLASS and we used the most recent auxiliary information. This study sets the stage for

395 future possible improvements. One example is land classification which currently is static. Another issue

396 is related to the representation of real time aerosol optical properties which are important under clear sky

397 conditions. It is believed that only now when NOAA/STAR has a stable aerosol retrieval algorithm, it

398 would be timely to address the aerosol issue in the estimation of TOA fluxes under clear sky.

399

400

401 Data availability. The data are available upon request from the corresponding author.

402 Author contributions. The investigation and conceptualization were carried out by RTP, IL and JD. YM
403 and WC developed the software. RTP prepared the original draft. All authors contributed to the writing,
404 editing and review of the publication.

405 Competing interests. The authors declare that they have no conflict of interest.

406 Disclaimer. Publisher's note: Copernicus Publications remains neutral with regard to jurisdictional claims
407 in published maps and institutional affiliations.

408 Acknowledgements. We acknowledge the benefit from the use of the numerous data sources used in this
409 study. These include the Clouds and the Earth's Radiant Energy System (CERES) teams, the Fast
410 Longwave and Shortwave Radiative Flux (FLASHFlux) teams, the
411 University of Wisconsin-Madison, Space Science and Engineering Center, Cooperative Institute for
412 Meteorological Satellite Studies (CIMSS) for providing the SeeBor Version 5.0 data
413 (https://cimss.ssec.wisc.edu/training_data/, and the final versions of the GOES Imager data were
414 downloaded from https://www.bou.class.noaa.gov/. Several individuals have been involved in the early
415 stages of the project whose contribution led to the refinements of the methodologies. These include M.
416 M. Woncsick and Shuyan Liu. We thank the anonymous Reviewers for a very thorough and constructive
417 comments that helped to improve the manuscript. We thank the Editor Sebastian Schmidt for overseeing
418 the disposition of the manuscript.
419

420 Financial support. This research was supported by NOAA/NESDIS GOES-R Program under grants
421 5275562 1RPRP_DASR and 275562 RPRP_DASR_20 to the University of Maryland.

422

423

Reference:

Akkermans T., and Clerbaux, N.: Narrowband-to-Broadband Conversions for Top-of-Atmosphere
  Reflectance from the Advanced Very High-Resolution Radiometer (AVHRR),
  Remote Sens. 12 (2), 305; https://doi.org/10.3390/rs12020305, 2020.

Berk, A., Bernstein, L. W., and Robertson, D. C.: MODTRAN: A moderate resolution model for
  LOWTRAN 7, Philips Laboratory, Report AFGL-TR-83-0187, Hanscom AFB, MA, 1985.

Berk, A., G. P. Anderson, P. K., Acharya, D. C. Robertson, J. H. Chetwynd, S. M. Adler-Golden:
  MODTRAN Cloud and Multiple Scattering Upgrades with Application to AVIRIS, Remote Sensing
  of Environment, 65 (3), 367-375, https://doi.org/10.1016/S0034-4257(98)00045-5, 1998.

Baldridge, A. M., Hook, S. J., Grove, C. I., Rivera, G.: The ASTER spectral library version 2, Remote
  Sensing of Environment 113, doi: 10.1016/j.rse.2008.11.007, 2009.

Borbas, E. E., Seemann, S. W., Huang, H.-L., Li, J., and Menzel, W. P.: Global profile training database
  for satellite regression retrievals with estimates of skin temperature and emissivity. Proceedings of
  the XIV, International ATOVS Study Conference, Beijing, China, University of Wisconsin-
  Madison, Space Science and Engineering Center, Cooperative Institute for Meteorological Satellite
  Studies (CIMSS), Madison, WI, pp.763-770, 2005.

Clerbaux, N., Russell, J. E., Dewitte, S., Bertrand, C., Caprion, D., De Paepe, B., Sotelino, L. G., Ipe, A.,
  Bantges, R., and Brindley, H. E.: Comparison of GERB instantaneous radiance and flux products
  with CERES Edition-2 data, Rem. Sens. of Environ., **113**, 102-114. doi:
  10.1016/j.rse.2008.08.016, 2009.

Cornette, W. M., Acharya, P. K., Robertson, D. C., and Anderson, G. P.: Moderate Spectral Atmospheric
  Radiance and Transmittance Code *(MOSART)*, Rep. R-057-94 (11–30), La Jolla, CA: Photon
  Research Associates, 1994.

Gristey, J. J., Su, W., Loeb, N. G., Vonder Haar, T. H., Tornow, F., Schmidt, K. S., Hakuba, M. Z.,

Pilewskie, P., Russell, J. E.: Shortwave Radiance to Irradiance Conversion for Earth Radiation Budget Satellite Observations: A Review, Remote Sens. 13, 2640, https://doi.org/10.3390/rs13132640, 2021.

Kato, S., Loeb, N. G., Rutan, D. A., Rose, F. G.: Clouds and the Earth's Radiant Energy System (CERES) Data Products for Climate Research Journal of the Meteorological Society of Japan, 93 (6), 597−612, DOI:10.2151/jmsj.2015-048, 2015.

Kratz, D. P., Stackhouse Jr., P. W., Gupta, S. K., Wilber, A. C., Sawaengphokhai, P., and McGarragh, G. R.: The Fast Longwave and Shortwave Flux (FLASHFlux) Data Product: Single-Scanner Footprint Fluxes, J. Appl. Meteor. Climatol., 53, 1059-1079, doi: 10.1175/JAMC-D-13-061.1, 2014.

Hansen, M. C., Defries, R. S., Townshend, J. R. G., and Sohlberg, R.: Global land cover classification at 1km spatial resolution using a classification tree approach, International Journal of Remote Sensing, 21(6-7):1331 – 1364, DOI:10.1080/014311600210209 https://doi.org/10.1080/014311600210209, 2010.

Harries, J. E., Russell, J. E., Hanafin, J. A., Brindley, H., Futyan, J., Rufus, J., Kellock, S., G. Matthews, R. Wrigley, A. Last, J. Mueller, R. Mossavati, J. Ashmall, E. Sawyer, D. Parker, M. Caldwell, P M. Allan, A. Smith, M. J. Bates, B. Coan, B. C. Stewart, D. R. Lepine, L. A. Cornwall, D. R. Corney, M. J. Ricketts, D. Drummond, D. Smart, R. Cutler, S. Dewitte, N. Clerbaux, L. Gonzalez, A. Ipe,C. Bertrand, A. Joukoff, D. Crommelynck, N. Nelms, D. T. Llewellyn-Jones, G. Butcher, G. L. Smith, Z. P Szewczyk, P E. Mlynczak, A. Slingo, R. P. Allan, and M. A. Ringer: The Geostationary Earth Radiation Budget Project, Bull. Amer. Meteor. Soc. 86 (7): 945, doi: 10.1175/BAMS-86-7-945, 2005.

Isaacs, R. G., W.-C. Wang, R. D. Worsham, and S. Goldenberg, S.: Multiple scattering LOWTRAN and FASCODE models. Applied Optics, 26(7), 1272 – 1281, 1987.

Kato, S., and Loeb, N. G.: Top-of-atmosphere shortwave broadband observed radiance and estimated irradiance over polar regions from Clouds and the Earth's Radiant Energy System (CERES) instruments on Terra, J. Geophys. Res., 110, D07202, doi:10.1029/2004JD005308, 2005.

475 Laszlo, I., Liu, H., Kim, H.-Y., and Pinker, R. T. : GOES-R Advanced Baseline Imager (ABI) Algorithm
476   Theoretical Basis Document (ATBD) for Downward Shortwave Radiation (Surface), and Reflected
477   Shortwave Radiation (TOA), version 3.1, Available at https://www.goes-r.gov/resources/docs.html,
478   2018.

479 Laszlo, I., Liu, H., Kim, H.-Y., and Pinker, R. T.: Shortwave Radiation from ABI on the GOES-R Series,
480   in: *The GOES-R Series*, edited by S. J. Goodman, T. J. Schmit, J. Daniels and R. J. Redmon. 179-191,
481   Elsevier, doi: https://doi.org/10.1016/B978-0-12-814327-8.00015-9, 2020.

482 Loeb, N. G., Smith, N. M., Kato, S., Miller, W. F., Gupta, S. K., Minnis, P. and Wielicki, B. A.: Angular
483   Distribution Models for Top-of Atmosphere Radiative Flux Estimation from the Mission Satellite,
484   Part I: Methodology, Journal of Applied Meteorology, 42 240-265, 2003.

485 Loeb N. G. et al.: Angular distribution models for top-of- atmosphere radiative flux estimation from the
486   Clouds and the Earth's Radiant Energy System Instrument on the Terra satellite. part I:
487   Methodology. J. Atmos. Oceanic Technol., 22:338–351, 2005.

488 Loveland T. R., B. C. Reed, J. F. Brown, D. O. Ohlen, Z. Zhu, L. Yang, J. W. Merchant: Development
489   of a global land cover characteristics database and IGBP DISCover from 1 km AVHRR data,
490   International Journal of Remote Sensing, 21 (6-7), 1303-1330, 2010.

491 Ma, Y., R. T. Pinker, M. M. Wonsick, C. Li, and L. M. Hinkelman: Shortwave radiative fluxes on
492   slopes. JAMC, 55, 1513-1532, https://doi.org/10.1175/*JAMC*-D-15-0178.1, 2016.

493 Ma, Y. and Pinker, R. T.: Shortwave Radiative Fluxes from Satellites: An Update. J. Geophys. Res.
494   Atmos**.**, 117, Issue D23, DOI: 10.1029/2012JD018332, 2012.

495 Niu, X. and Pinker, R. T.: Revisiting satellite radiative flux computations at the top
496   of the atmosphere, International Journal of Remote Sensing, DOI:10.1080/01431161.2011.571298,
497   2011.

498 Niu, X. and Pinker, R. T.: An improved methodology for deriving high resolution
499   surface shortwave radiative fluxes from MODIS in the Arctic region, J. Geophys. Res.
500   Atmos., 120, 2382–2393, doi: 10.1002/2014JD022151, 2015.

501 Pinker, R. T., Zhang B., Dutton E. G.: Do satellites detect trends in surface solar radiation? *SCIENCE*,
502   308, 5723, 850-854, 2005.
503 Pinker, R. T., A. Bentamy, B. Zhang, W. Chen, and Ma, Y.: The net energy budget at the ocean-
504   atmosphere interface of the ''Cold Tongue'' region, J. Geophys. Res. Oceans, 122, doi: 10.1002/
505   2016JC012581, 2017a.
506 Pinker, R. T., S. Grodsky, B. Zhang, A. Busalacchi, and Chen, W.: ENSO Impact on Surface Radiative
507   Fluxes as Observed from Space. J. Geophys. Res.-Oceans., doi: 10.1002/2017JC012900, 2017b.
508 Pinker, R. T., Zhang, B. Z., Weller, R. A., and Chen, W.: Evaluating surface radiation fluxes observed
509   from satellites in the southeastern Pacific Ocean. Geophysical Research Letters, 45.
510   https://doi.org/10.1002/2017GL076805, 2018.
511 Rajulapati, C. R., S. M. Papalexiou, M. P. Clark, and Pomeroy, J. W.: The Perils of Regridding:
512   Examples Using a Global Precipitation Dataset, Journal of Applied Meteorology and
513   Climatology, 60 (11), 1561–1573, doi: 10.1175/JAMC-D-20-0259.1, 2021.
514 Rilee M. L. and Kuo, K. S.: The Impact on Quality and Uncertainty of Regridding Diverse Earth
515   Science Data for Integrative Analysis, IN43C-0916, 2018.
516 Scarino et al.: A Web-Based Tool for Calculating Spectral Band Difference Adjustment Factors Derived
517   from SCIAMACHY Hyperspectral Data, IEEE Trans. Geo. Remote Sens., 54, 5,
518   10.1109/TGRS.2015.2502904, 2016.
519 Stamnes, K., S.-C. Tsay, W. Wiscombe and K. Jayaweera: Numerically stable algorithm for discrete-
520   ordinate-method radiative transfer in multiple scattering and emitting layered media, Applied
521   Optics, 27 (12), 2502–2509, 1988.
522 Su, W., Corbett, J., Eitzen, Z., and Liang, L.: Next-generation angular distribution models for
523   top-of-atmosphere radiative flux calculation from CERES instruments: methodology, Atmos.
524   Meas. Tech., 8, 611–632, https://doi.org/10.5194/amt-8-611-2015, 2015.
525 Wang, H; Pinker, R. T.: Shortwave radiative fluxes from MODIS: Model development and
526   implementation. JGR-Atmospheres, 114, D20201, 2009.

527 Wielicki, B. A.; Doelling, D. R.; Young, D. F.; Loeb, N. G.; Garber, D. P.; MacDonnell, D. G.: Climate

528   quality broadband and narrowband solar reflected radiance calibration between sensors in orbit.

529   In Proceedings of the IGARSS 2008 IEEE International Geoscience and Remote Sensing

530   Symposium, Boston, MA, USA, 7–11 July 2008.

531 Zhang, T., Stackhouse Jr., P. W., Cox, S. J., Mikovitz, J. C., Long, C. N.: Clear-sky shortwave

532   downward flux at the Earth's surface: Ground-based data vs. satellite-based data, Journal of

533   Quantitative Spectroscopy & Radiative Transfer, 224, 247-260, 2019,

534   www.elsevier.com/locate/jqsrt.

535
536
537
538

Tables

Table 1. Channel information and spectral bands for ABI.

ABI Band #	Central wavelength (μm)	Spectral band (μm)
1	VIS 0.47	0.45-0.49
2	VIS 0.64	0.60-0.68
3	NIR 0.86	0.847-0.882
4	NIR 1.38	1.366-1.380
5	NIR 1.61	1.59-1.63
6	NIR 2.26	2.22-2.27

539

540

541

542   Table 2. Surface classification description for IGBP 18 types, IGBP 12 types, CERES clear sky 6 types,

543   and NTB cloudy sky 4 types

IGBP (18 types)	IGBP (12 types)	CERES clear-sky (6 types)	NTB cloudy-sky (4 types)
Evergreen Needleleaf	Needleleaf Forest	Mod-High Tree/Shrub	Land
Deciduous Needleleaf			
Evergreen Broadleaf	Broadleaf Forest		
Deciduous Broadleaf			
Mixed Forest	Mixed Forest		
Closed Shrublands	Closed Shrub		
Woody Savannas	Woody Savannas		
Savannas	Savannas	Low-Mod Tree/Shrub	
Grasslands	Grasslands		
Permanent Wetlands			
Tundra			
Croplands	Croplands		
Open Shrublands	Open Shrub		
Urban and Built-up	Open Shrub	Dark Desert	Desert
Bare Soil and Rocks	Barren and Desert	Bright Desert	
Snow and Ice	Snow and Ice	Snow and Ice	Snow and Ice
Water Bodies	Ocean	Ocean	Water

544

545
546

547

548   Table 3. The various classes for which NTB coefficients are generated.

Parameter	Clear condition	Cloudy condition
Aerosol or cloud type	6 aerosol types (rural, maritime, urban, tropospheric, fog, desert)	3 cloud types (cirrus, stratocumulus, altostratus)
Optical depth (OD)	Typical VIS (km) values for each aerosol types (no OD grid for each aerosol type). Rural: 23, maritime: 23, urban: 5, tropospheric: 50, fog: 0.2, desert: (default VIS for wind speed 10m/s)	Cirrus: [0, 0.8, 1.2, 1.8, 3.2] Stratocumulus: [0, 0.8, 1.2, 1.8, 3.2, 5.8, 8.2, 15.8, 32.2, 51.8, 124.2] Altostratus: [0, 15.0, 30.0, 50.0, 80.0]
Surface type	12 IGBP surface types	4 types (Water, Land, Desert, Snow/Ice)

549

550

551

552

553   Table 4. Angles used in simulations. To be consistent with what is presented in the

554   ABI Shortwave Radiation Budget (SRB) Algorithm Theoretical Basis Documents (ATBD) (Laszlo

555   et al, 2018) the additional angles used in the simulations are not given in this Table.

Angle Type	Angles
Solar Zenith Angle [°]	0.0, 12.9, 30.8, 41.2, 48.3, 56.5, 63.2, 69.5, 75.5, 81.4, 87.2
Satellite Zenith Angle [°]	0.0, 11.4, 26.1, 40.3, 53.8, 65.9, 76.3
Azimuth Angle [°]	0.0, 1.9, 10.0, 24.2, 44.0, 68.8, 97.6, 129.3, 162.9, 180

556

557

558

559

560

Table 5. MODTRAN simulation speed test (CPU MHz 2099.929).

Algorithm	Stream	Band Resolution (cm^{-1})	Speed (~seconds)
Isaacs	2	1	40
DISORT	2	1, 5, 15	280, 70, 30
	4	1, 5, 15	560, 120, 40
	8	1, 5, 15	930, 300, 110
Scaled Isaac	2	1, 5, 15	30, 10, 6.67
	4	1, 5, 15	30, 10, 6.67
	8	1, 5, 15	30, 10, 6.67

561

562

563

564

565 Table 6. Details on data used as input for calculations.

566

Short Name	Long Name	MODE	ABI-Channel	Scan Sector	Spatial Resolution
RadC	L1b Radiance	M6	C01-C06	CONUS	5000x3000
AODC	L2 Aerosol	M6	--	CONUS	2500x1500
ACMC	L2 Clear Sky Masks	M6	--	CONUS	2500x1500
ACTPC	L2 Cloud Top Phase	M6	--	CONUS	2500x1500
CODC*	L2 Cloud Optical Depth	M6	--	CONUS	2500x1500

567
568

569

Table 7. Statistical summary for all selected cases intercompared at instantaneous time   scale.

Case	CERES	GOES-R	Corr	Bias	Std	RMSE	N
07/31 2019 UTC 19	Terra	G16	0.82	0.81	69.81	69.81	0.22×10^6
		G17	0.87	29.13	90.10	94.70	1.78×10^6
	Aqua	G16	0.76	33.87	117.43	122.22	1.58×10^6
		G17	0.78	31.53	129.42	133.21	0.29×10^6
09/13 2019 UTC 20	Terra	G16	0.87	-17.37	81.72	83.54	0.13×10^6
		G17	0.71	47.09	108.73	118.48	1.73×10^6
	Aqua	G16	0.76	18.22	108.50	110.02	1.46×10^6
		G17	0.73	25.14	81.95	85.72	0.53×10^6
09/21 2019 UTC 19	Terra	G16	0.85	6.78	66.66	67.00	0.35×10^6
		G17	0.83	26.41	87.64	91.57	1.75×10^6
	Aqua	G16	0.82	29.66	105.09	109.20	1.67×10^6
		G17	0.76	6.03	94.70	94.89	0.15×10^6
09/30 2019 UTC 19	Terra	G16	0.88	4.49	64.79	64.94	0.40×10^6
		G17	0.80	19.35	86.41	88.55	1.74×10^6
	Aqua	G16	0.80	19.87	100.45	102.40	1.69×10^6
		G17	0.72	2.71	91.79	91.83	0.12×10^6
	Terra	G16	0.86	5.84	51.44	51.77	0.35×10^6

Date	Satellite					
10/23 2019 UTC 19		G17	0.87	22.47	70.25	73.76	1.75×10^6
	Aqua	G16	0.89	17.10	75.95	77.85	1.67×10^6
		G17	0.78	8.98	72.52	73.07	0.15×10^6
11/08 2019 UTC 19	Terra	G16	0.87	-0.50	43.28	43.28	0.35×10^6
		G17	0.82	17.18	71.27	73.31	1.75×10^6
	Aqua	G16	0.90	10.08	71.27	71.98	1.67×10^6
		G17	0.68	1.53	47.55	47.58	0.15×10^6
11/24 2019 UTC 19	Terra	G16	0.79	7.98	49.10	49.75	0.35×10^6
		G17	0.87	14.10	78.35	79.61	1.76×10^6
	Aqua	G16	0.82	7.63	58.68	59.17	1.67×10^6
		G17	0.65	0.19	63.14	63.14	0.15×10^6
12/26 2019 UTC 19	Terra	G16	0.88	5.24	53.28	53.54	0.35×10^6
		G17	0.76	11.26	73.95	74.80	1.76×10^6
	Aqua	G16	0.83	9.79	58.90	59.56	1.67×10^6
		G17	0.73	0.85	52.53	52.54	0.15×10^6

571
572
573
574
575
576
577
578
579

580   List of Figures

606   Figure 14. Same as Figure 11 but for cloudy TOA SW differences.

607   Figure 15. *Left:* Sensor response function for ABI channel 6; *Right:* Spectral albedo for desert and open
608   shrubs. Desert albedo value is much higher than open shrubs at 2.2 µm.

609

610
611
612

613

614
615
616
617
618
619
620
621
622
623
624
625
626
627
628
629
630
631
632
633
634
635
636
637
638
639
640
641
642

643 **Figures**

644

645
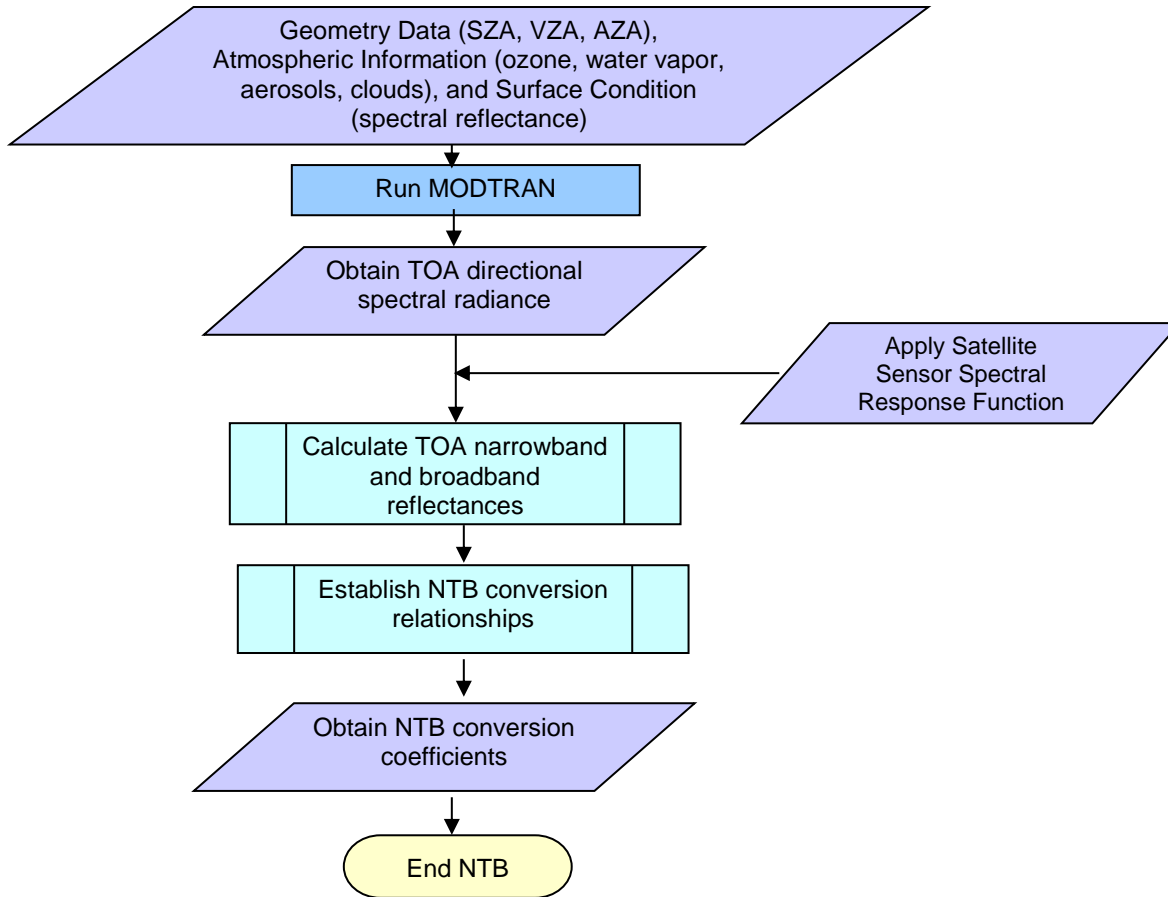
646

647 Figure 1. Flowchart of the NTB transformations illustrating the main processing sections.

648

649

650
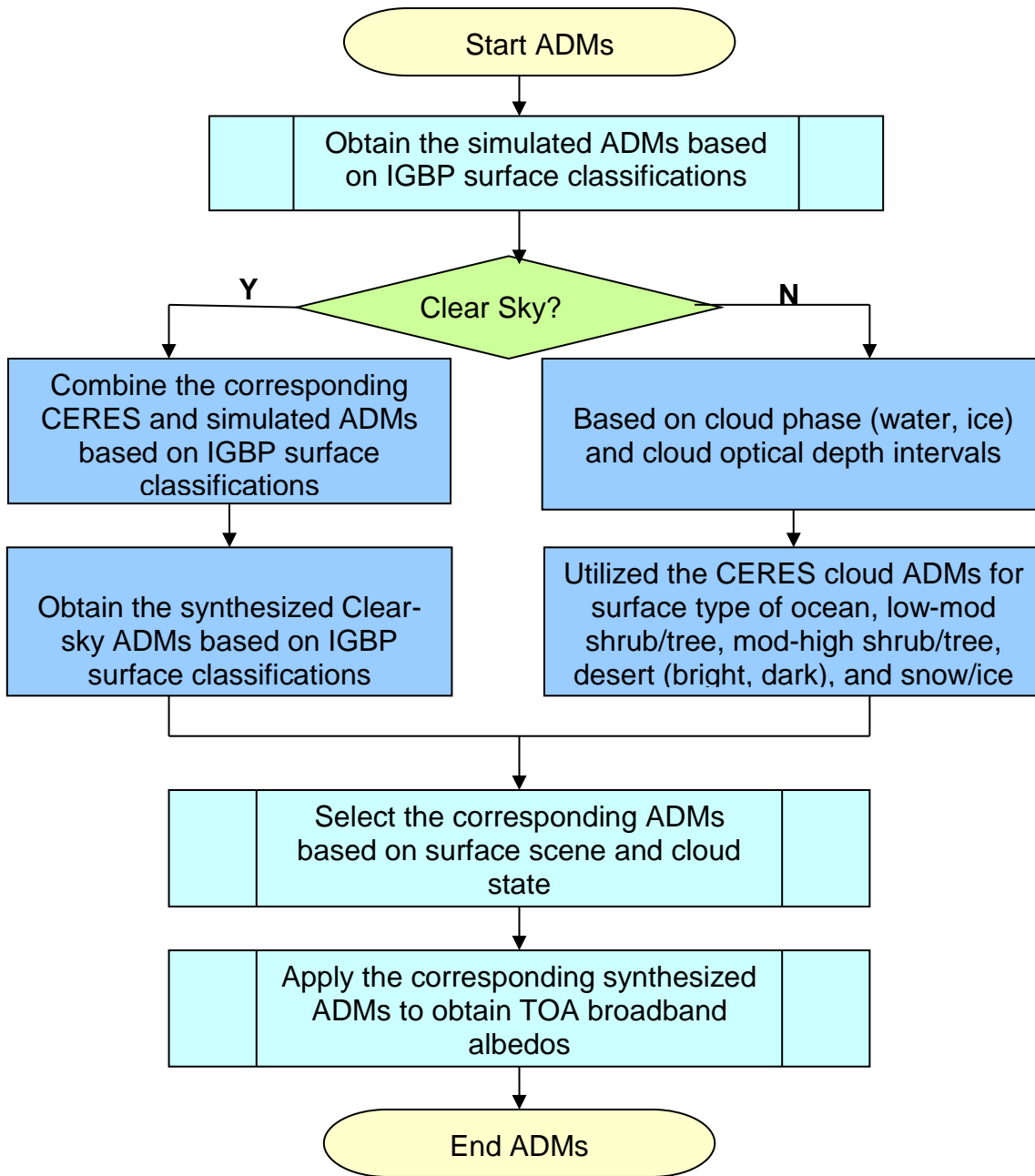
651

652   Figure 2. Schematic illustration of the logic employed to synthesize modeled and observed ADMs.

653

654

655

656
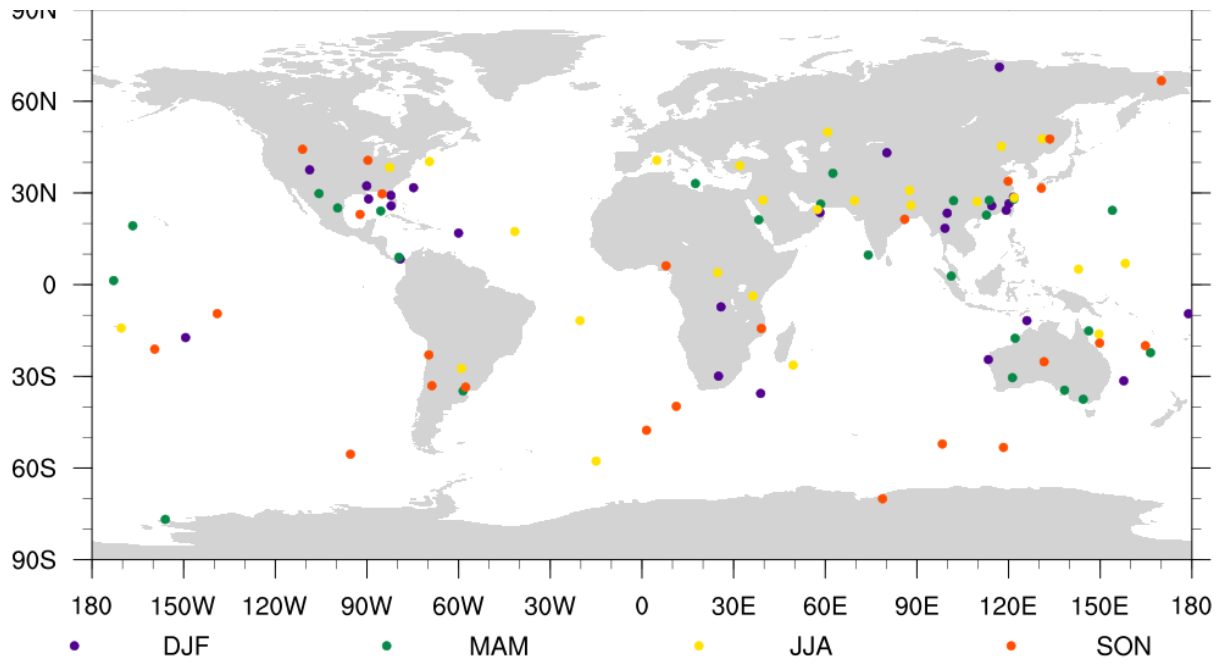
Figure 3. The location of the 100 selected clear sky profiles from SeeBor used in the simulations.

659

660
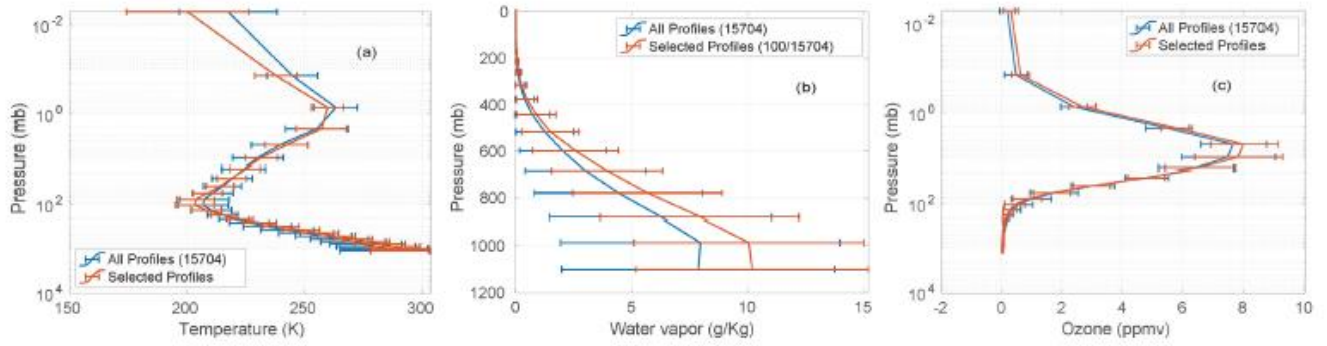
661

662 Figure 4. Profile statistics of: (a) temperature; (b): water vapor; (c) ozone for the entire available sample
663 and for the reduced sample used in this study. Error bar is 1 standard deviation.

664

665

666
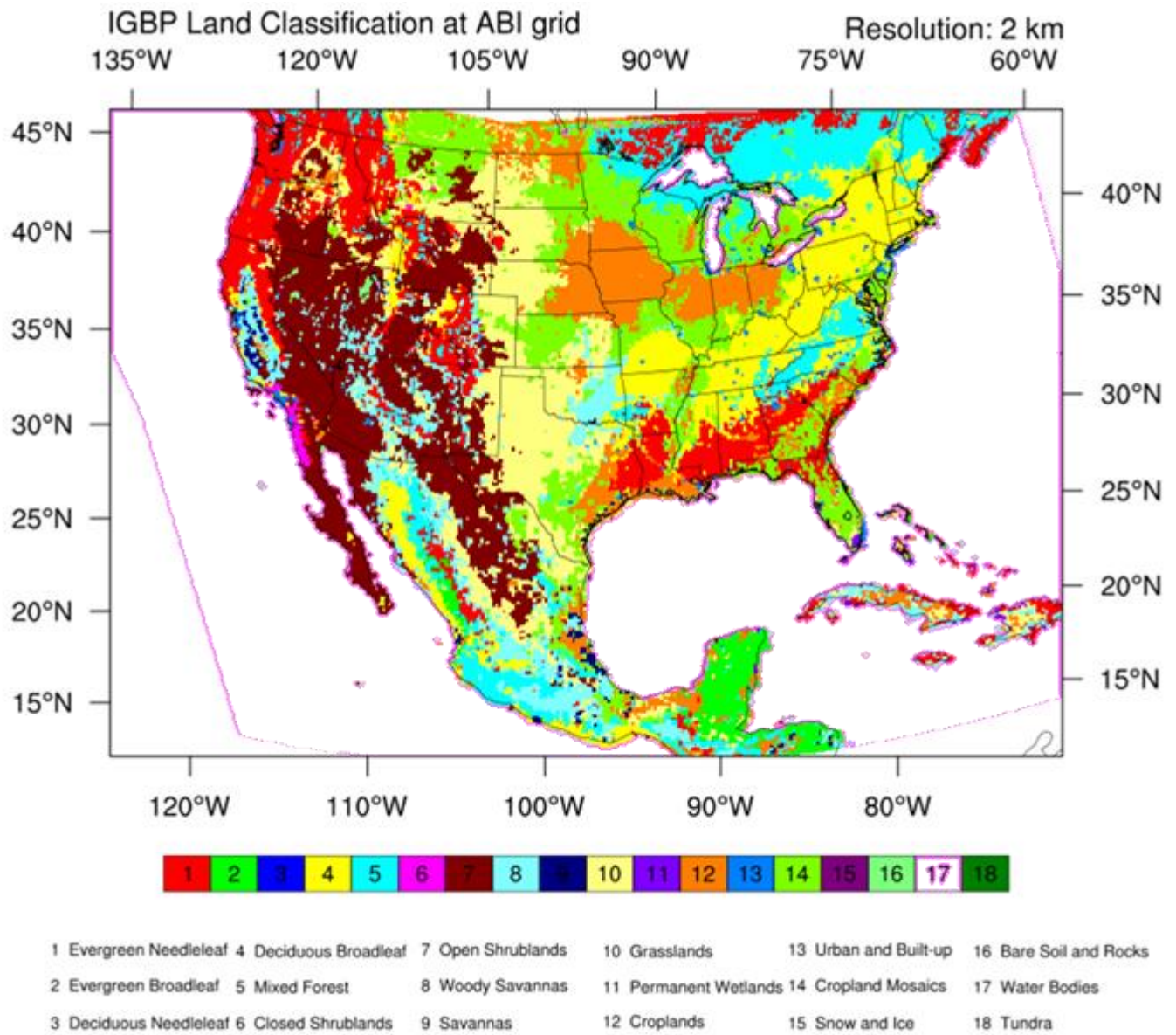
667

668   Figure 5. Re-mapped IGBP surface classifications over the CONUS at 2-km ABI grid.

669

670

671

672
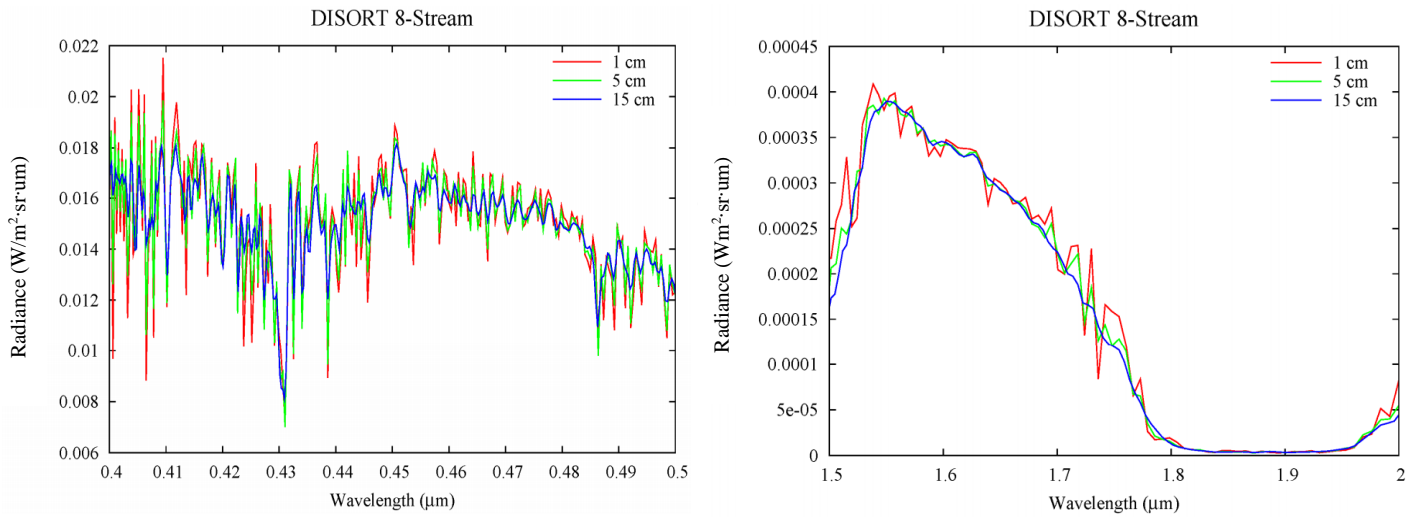
Figure 6. Simulated Radiances from DISORT 8-stream (with 1, 5, and 15 cm^{-1} resolution band

model for spectral range of 0.4 – 0.5 µm (left) and 1.5 – 2.0 µm (right).

675

676

677

678
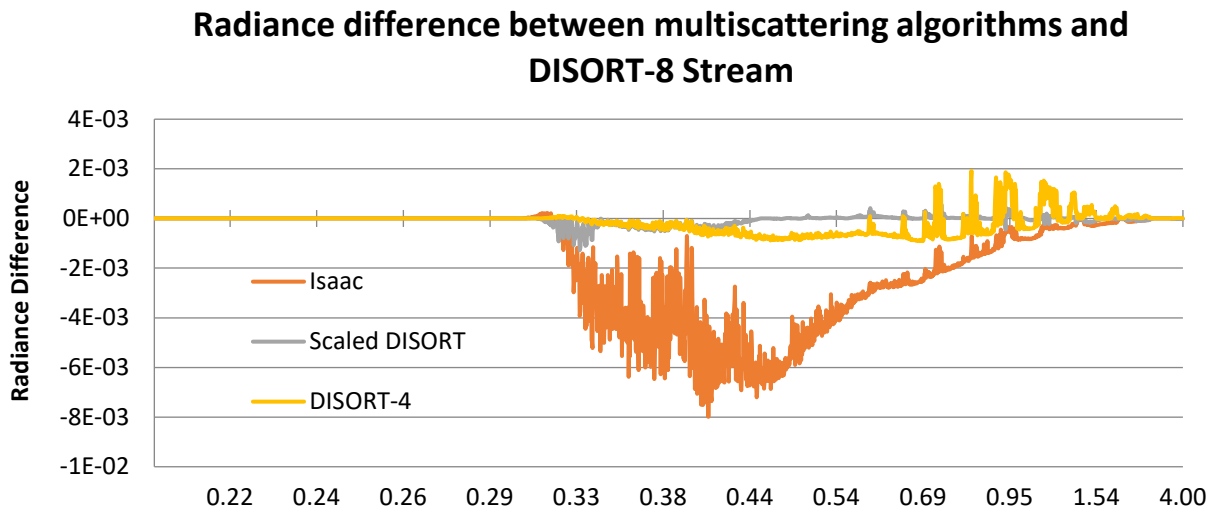
679
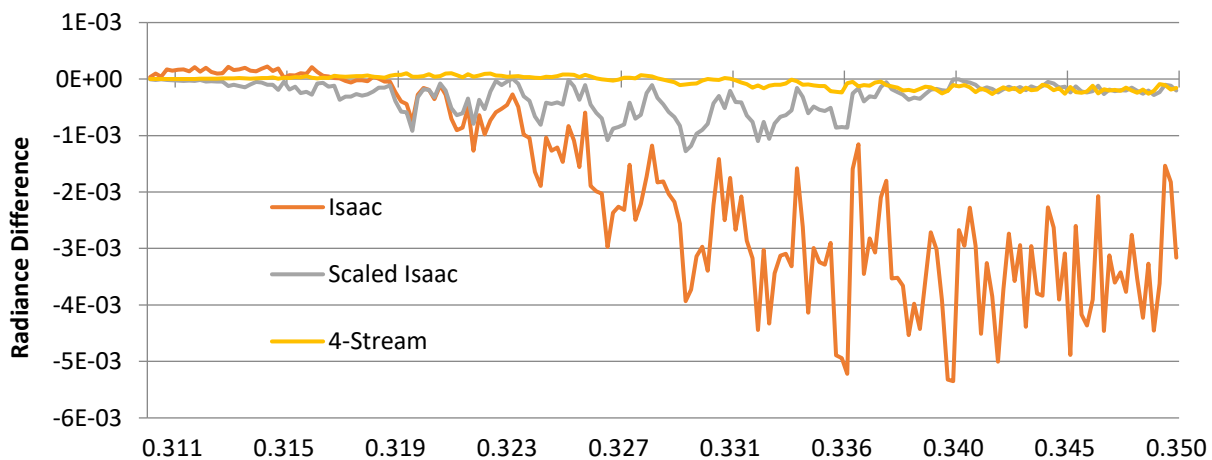
680

681   Figure 7. Radiance differences between various multi-scattering algorithms and DISORT-8 stream.

682   *Upper*: the whole simulated spectrum of 0.2-4 µm; *Lower:* zoom on 0.3-0.35 µm (Relative

683   Azimuthal Angle=1.9°, View Angle=76.3°, Solar Zenith Angle=87.2°).

684
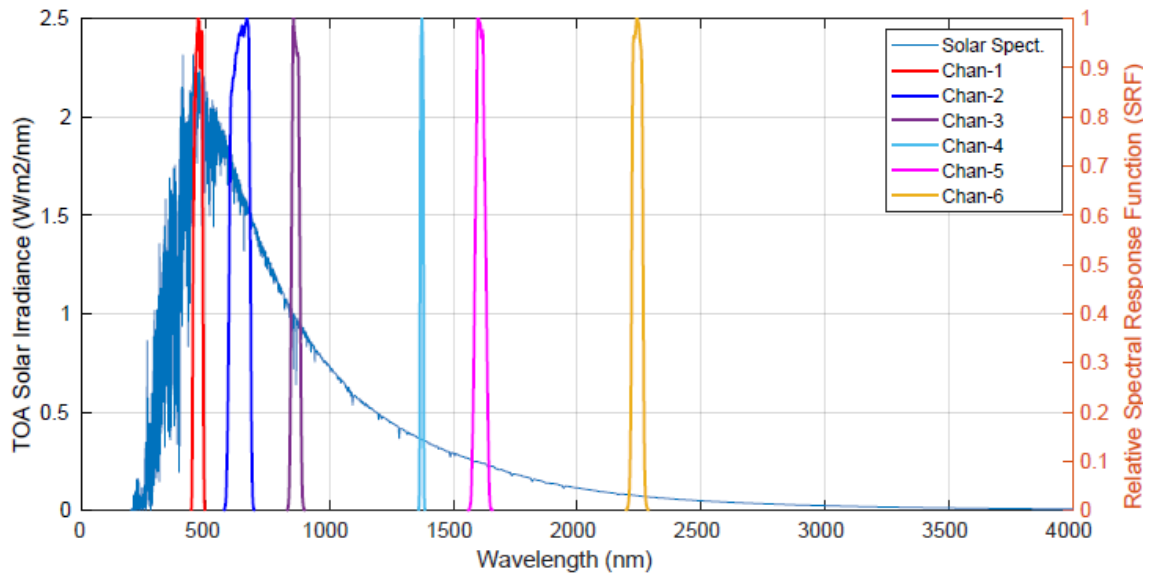
685

686

687   Figure 8. Locations of the six ABI channel SRFs. X-axis is wavenumber. Y-axis is solar irradiance.

688
689

690

691
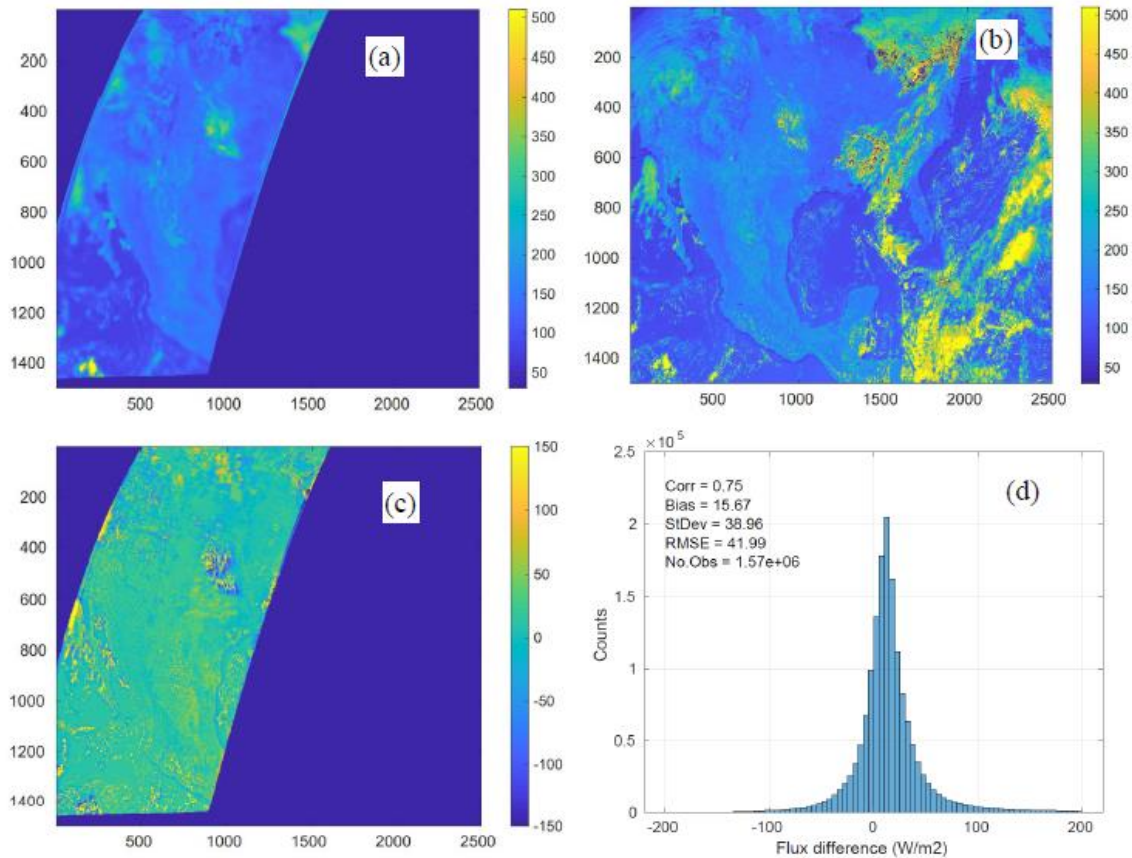
692

693 Figure 9. Comparison of TOA flux from ABI and CERES FLASHFlux for 2017/11/25, 17:57Z. (a)

694   CERES Terra product; (b): results with "separate-channel" coefficients. (c): difference (ABI-

695   CERES); (d): histogram of ABI-CERES differences (this is the only case illustrated in this paper

696   with data from FLASHFlux).

697

698

699
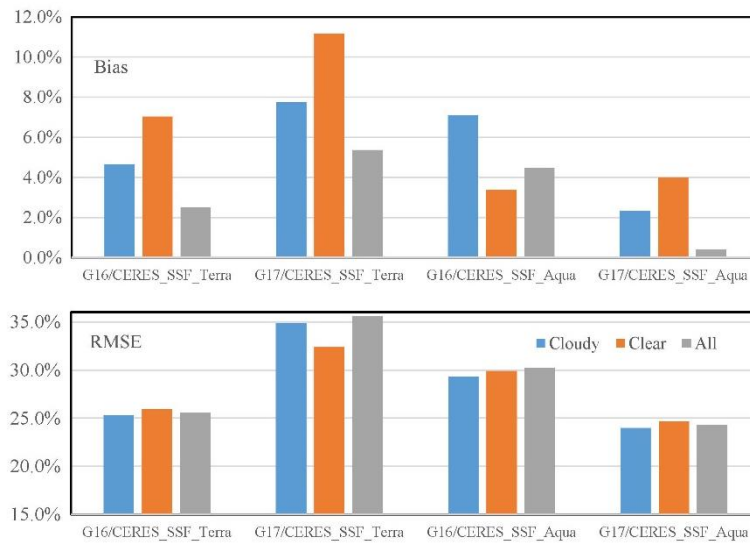
700
701
702   Figure 10. Statistics for relative Bias and RMSE. The y-axis is percentage. The x-axis is the case used in
703   the inter-comparison. Blue - cloudy orange - clear sky and t gray - all sky.

704

705

706

707

708

709

710

711

712
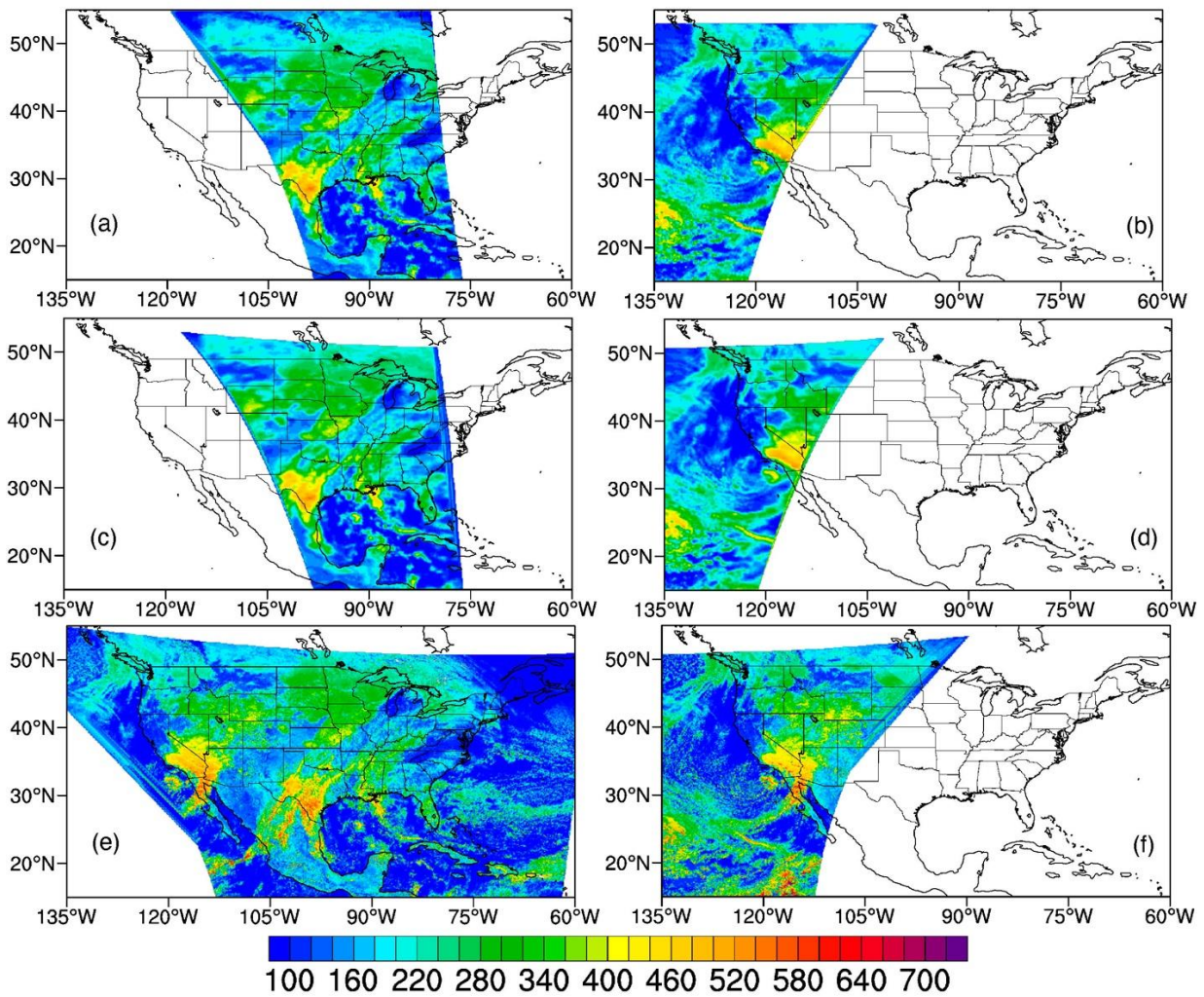
Figure 11. (a) All sky TOA SW from CERES_SSF/Aqua, (b) CERES_SSF/Terra, (c) re-gridded
CERES_SSF/Aqua, (d) re-gridded CERES_SSF/Terra, (e) GOES-16 and (f) GOES-17
on 12/26/2019 at UTC 19:36.
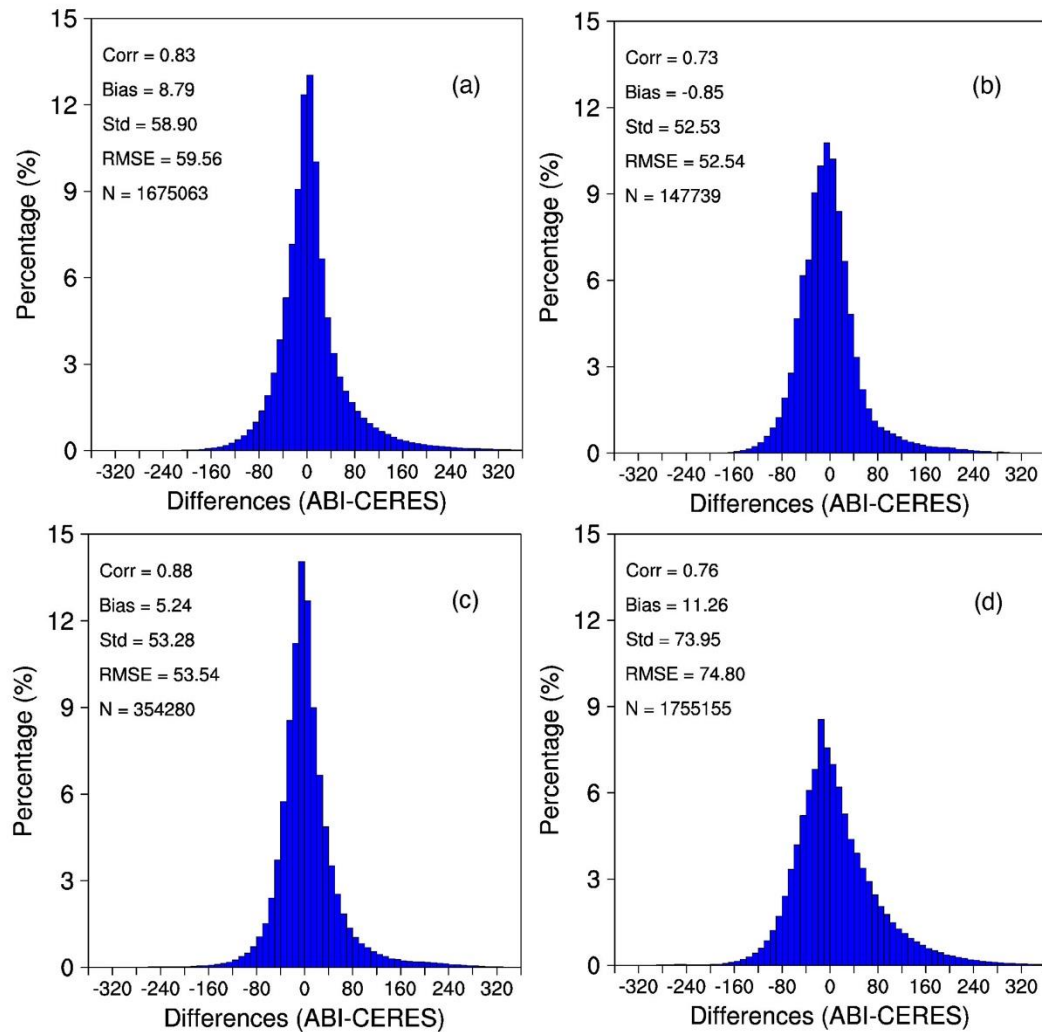
Figure 12. (a) Frequency distribution of all-sky TOA SW differences between ABI on GOES-16
and CERES, (b) ABI on GOES-17 and CERES_SSF using Aqua (Upper) and Terra
(Lower). All observations were used (clear and cloudy) on 12/26/2019 at UTC 19:36.

723
724
725
726
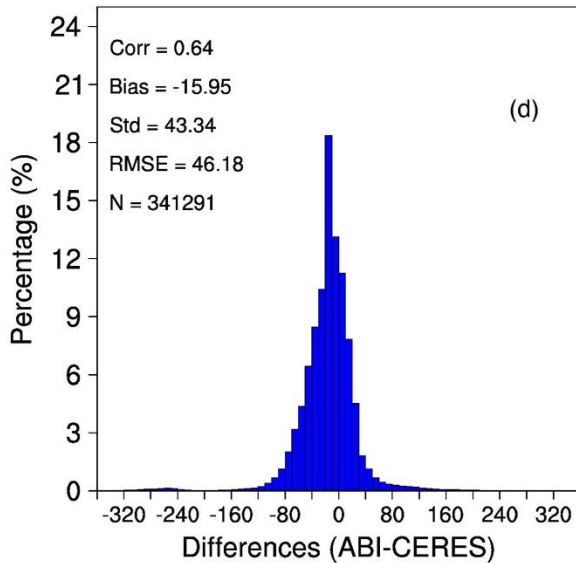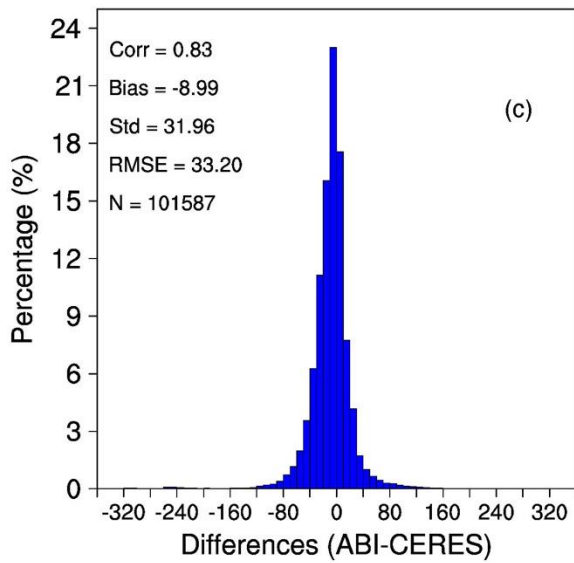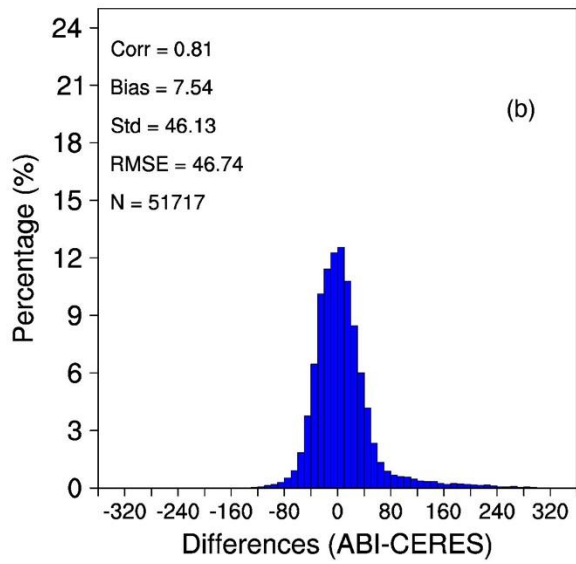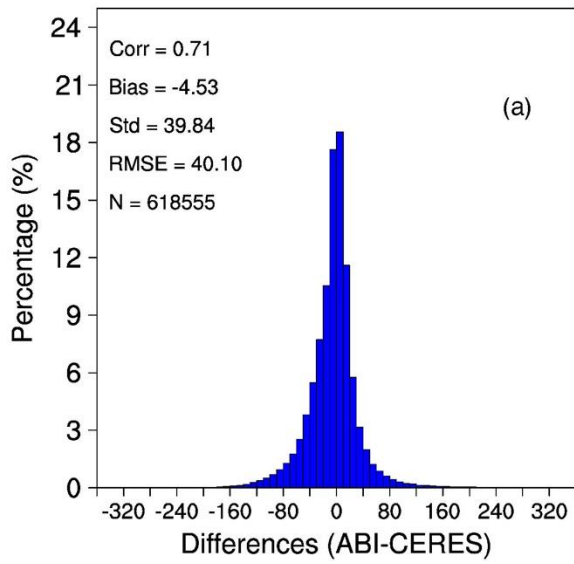
727
728   Figure 13. Same as Figure 11 but for clear TOA SW differences.
729
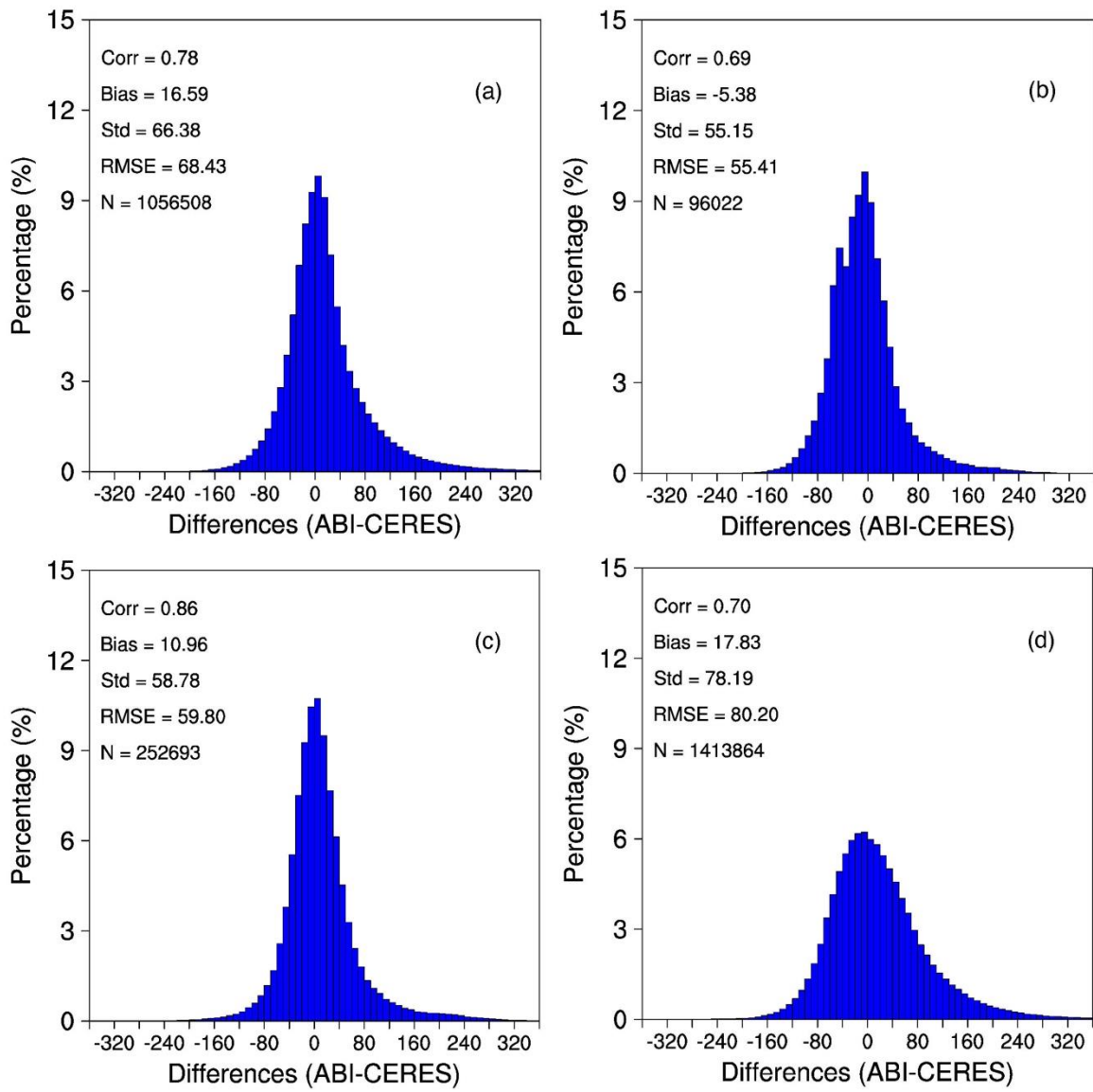
730
731 Figure 14. Same as Figure 11 but for cloudy TOA SW differences.
732
733

734
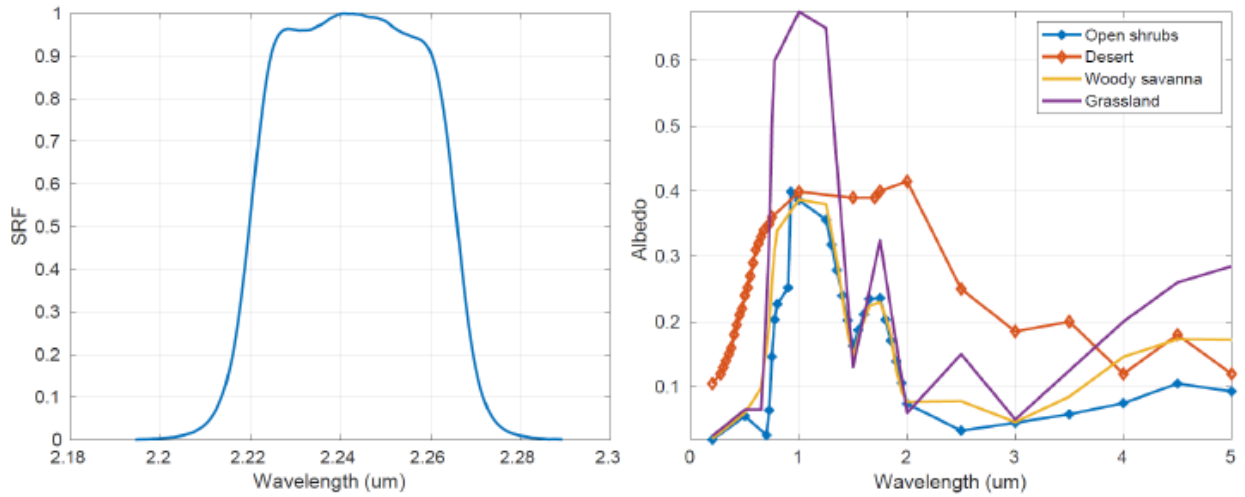
735

736   Figure 15. *Left:* Sensor response function for ABI channel 6; *Right:* Spectral albedo for desert and open

737   shrubs. Desert albedo value is much higher than open shrubs at 2.2 µm.

738

739